Plasma Heating and Alfvénic Turbulence Enhancement During Two Steps of Energy Conversion in Magnetic Reconnection Exhaust Region of Solar Wind

He Jiansen[1], Zhu Xingyu[1], Chen Yajie[1], Salem Chadi[2], Stevens Michael[3], Li Hui[4],
Ruan Wenzhi[1,5], Zhang Lei[4], and Tu Chuanyi[1]
[1] School of Earth and Space Sciences, Peking University, Beijing, 100871, People's Republic of China; jshept@pku.edu.cn
[2] Space Sciences Laboratory, University of California, Berkeley, CA 94720, USA
[3] Harvard-Smithsonian Center for Astrophysics, Cambridge, MA 02138, USA
[4] State Key Laboratory of Space Weather, National Space Science Center, CAS, Beijing, 100190, People's Republic of China
[5] Centre for Mathematical Plasma Astrophysics, KU Leuven, B-3001 Heverlee, Belgium

Abstract

The magnetic reconnection exhaust is a pivotal region with enormous magnetic energy being continuously released and converted. The physical processes of energy conversion involved are so complicated that an all-round understanding based on in situ measurements is still lacking. We present the evidence of plasma heating by illustrating the broadening of proton and electron velocity distributions, which are extended mainly along the magnetic field, in an exhaust of interchange reconnection between two interplanetary magnetic flux tubes of the same polarity on the Sun. The exhaust is asymmetric across an interface, with both sides being bounded by a pair of compound discontinuities consisting of rotational discontinuity and slow shock. The energized plasmas are found to be firehose unstable, and responsible for the emanation of Alfvén waves during the second step of energy conversion. It is realized that the energy conversion in the exhaust can be a two-step process involving both plasma energization and wave emission.

Key words: magnetic reconnection – solar wind – turbulence

1. Introduction

Magnetic reconnection is a crucial process of tremendous energy release in various magnetized plasma environments in which magnetic energy is converted into plasma bulk, thermal, and non-thermal kinetic energy. It is in the solar wind that one can measure in situ the physical processes in an extended exhaust region far away from the x-line of magnetic reconnection, and that one can learn to what extent the reconnected topology and the associated discontinuities can influence the plasma kinetics and wave activities.

Magnetic reconnection in the magnetohydrodynamic (MHD) regime is usually considered and simulated to have a pair of rotational discontinuities (RDs) and a pair of slow shocks (SSs) bounding the exhaust region (Petschek 1964; Sonnerup 1979; Lin & Lee 1995). The fast reconnection process has been successfully modeled more recently with Hall-MHD, hybrid, and full particle-in-cell simulations (Birn et al. 2001). However, unlike MHD modeling, probably due to the size limitation (usually less than hundreds of proton inertial length) of simulation box, kinetic simulation can hardly reproduce the discontinuities, e.g., RDs and SSs (Innocenti et al. 2015).

Interplanetary reconnection exhausts are commonly identified in slow solar wind observations and occasionally in the fast streams as well (Gosling et al. 2005a; Phan et al. 2006; Gosling et al. 2007; Vörös et al. 2014). Reconnection can change the topology of the interplanetary magnetic field (IMF) lines by interchanging their footpoints on the Sun (Crooker et al. 2012), by cutting their connection to the Sun (Gosling et al. 2005b), or by altering their connectivity among multiple disconnected structures. Simultaneous measurements by several spacecraft have shown that magnetic reconnection in the solar wind can present as a quasi-steady state and a large-scale process in terms of the x-line length (Phan et al. 2006). A profile with two steps of monotonic jump in the magnetic shear component,

(B_L), is often present across the solar wind reconnection exhaust. This profile differs from the gradual transition in the magnetic shear component that is often the signature of magnetotail reconnection (Eastwood et al. 2010). In association with the two-step jump in B_L, the corresponding velocity component (V_L) shows two steps of opposite jump (up–down or down–up), indicating the existence of a pair of RDs. These RDs propagate primarily along with the jet flow at about Alfvén speed, V_A, as well as apart from one another into the external upstream region. Slow shocks in space plasmas have been identified in spacecraft data (Lin et al. 2008) and have been found to adjoin with an RD some times (Whang et al. 1998; Eriksson et al. 2004).

Ions and electrons are found to be hotter in the exhaust region than the average of the temperatures outside of it. The hot protons tend to be thermally anisotropic, with $T_\parallel$ being larger than $T_\perp$ (Gosling et al. 2005a; Huttunen et al. 2007). It has been predicted by kinetic simulations and confirmed in statistical observations that the increment of the ion temperature is proportional to both the ion mass and the squared exhaust velocity (Drake et al. 2009). The anisotropic heating of electron cores seems to be more evident in the events with higher inflow Alfvén speed (Pulupa et al. 2014). Electron energization in the ion diffusion region manifests as a flat-top distribution with a pair of trapping-passing boundaries that separate the trapped electrons (trapped not only by the magnetic field but also by the electric potential) and the passing electrons with small pitch angles (Egedal et al. 2008, 2012).

In the ion diffusion region, whistler waves can be excited locally, with free energy coming from the non-Maxwellian phase space distribution of the electrons (Deng & Matsumoto 2001; Fujimoto & Sydora 2008), and electron vortex flow may also be formed due to the Kelvin–Helmholtz instability of
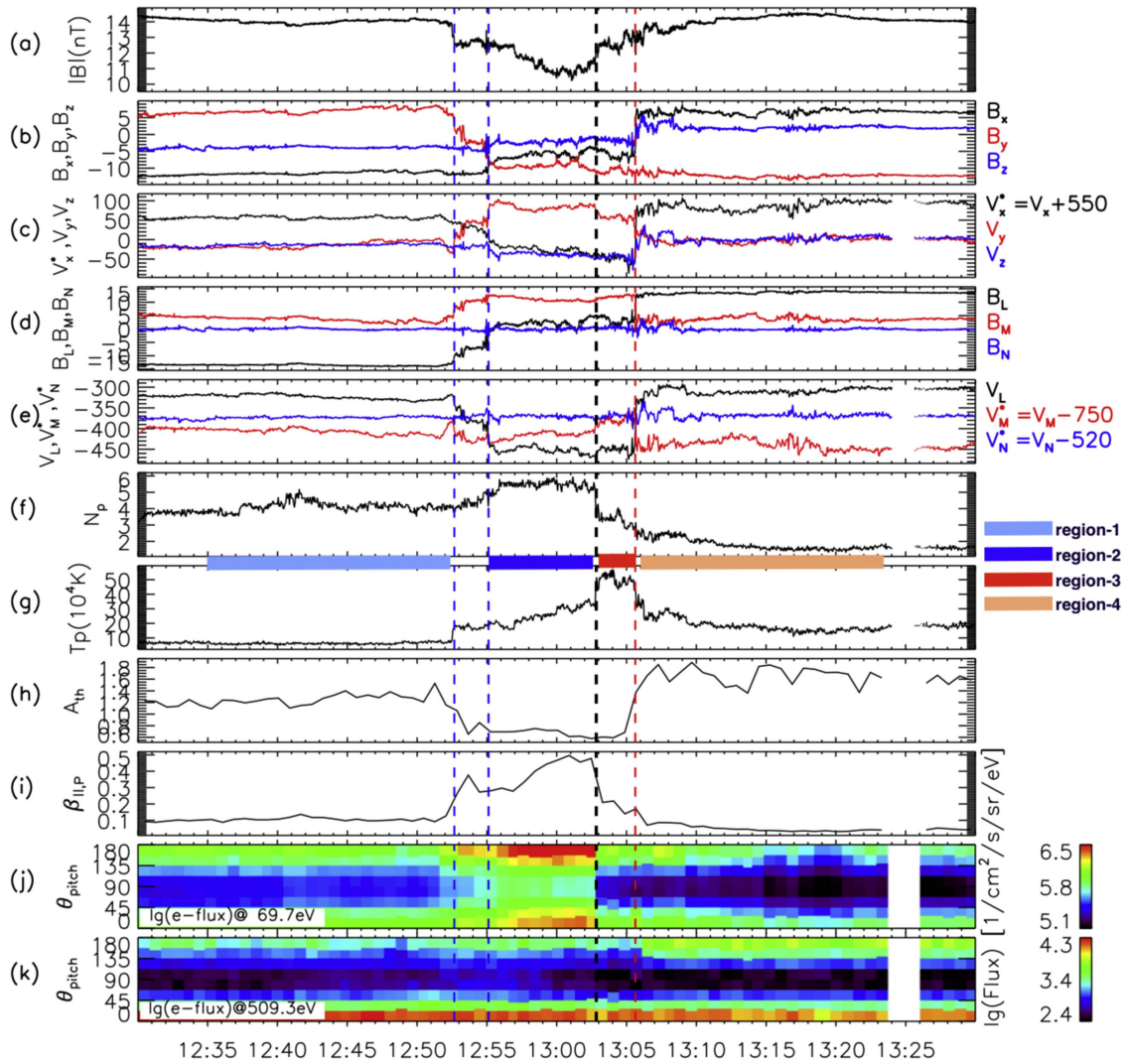
Figure 1. Overview of plasma and magnetic field measurements between 12:30 and 13:30 on 1997 November 23. Time sequences of the magnetic field strength |B| , the magnetic field components in the GSE coordinates (B_x, B_y, B_z), and the transformation results in the global LMN coordinates (B_L, B_M, B_N) are plotted in panels (a), (b), and (d), respectively. Solar wind proton bulk velocity vectors (V_x, V_y, V_z) and (V_L, V_M, V_N) are displayed in panels (c) and (e). The density, temperature, thermal anisotropy, and parallel plasma β of protons are plotted in panels (f), (g), (h), and (i), respectively. The electron differential flux density at the energy channels of about 70 eV and 509 eV are illustrated in panels (j) and (k). Two blue vertical dashed lines denote the positions of two rotational discontinuities (RDs) on the anti-sunward side of the exhaust. Another RD on the sunward side is denoted with a red vertical dashed line. The contact interface between the two different downstream regions is marked with a black dashed line. The cool upstream, cool downstream, warm downstream, and warm upstream regions are denoted with the light blue, blue, red, and orange bars, respectively.

the electron shear flow as drifted by the Hall electric field and guide magnetic field (Huang et al. 2015). Turbulence in the reconnection jet flow region is observed to have intermittent coherent structures (Vörös et al. 2004; Weygand et al. 2005; Huang et al. 2012), which seem to be the sites of concentrated dissipation (Osman et al. 2014). Firehose instability are found to be existent and mitigated by the developing waves/ turbulence in the 2D particle-in-cell simulated exhaust region, which is bounded by coplanar SSs and non-coplanar RDs.

In the jet, downstream and quite distant from the reconnection diffusion region, the proton and electron velocity distribution functions VDF($V_\parallel$, $V_\perp$), the key signatures of their thermal kinetics, have yet to be revealed simultaneously. What will happen to the plasma kinetics in the exhaust if the plasma states on both sides involved in the reconnection are asymmetric in number density and magnetic field strength, which is prevalent in various environments (Aschwanden et al. 1999; Øieroset et al. 2004; Liu et al. 2011)? Are the energized plasmas stable or

unstable in the exhaust region? If unstable, are they responsible for the second step of energy conversion by exciting and emanating waves? These unknown elements of importance to magnetic reconnection are to be addressed in this work.

2. Observations and Analyses

2.1. Discontinuities Bounding and Separating the Reconnection Exhaust

We choose a reconnection exhaust region in the solar wind that was encountered by the *ACE* and the *Wind* spacecraft on 1997 November 23 (Gosling et al. 2005a; Phan et al. 2009; Pulupa et al. 2014) for a comprehensive study. Figure 1 shows an overview of this event based on the plasma and magnetic field measurements. The magnetic field strength, |**B**|, is weakened at the trough in the time profile (Figure 1(a)). The |**B**| trough is bounded by a set of jumps in the vector magnetic
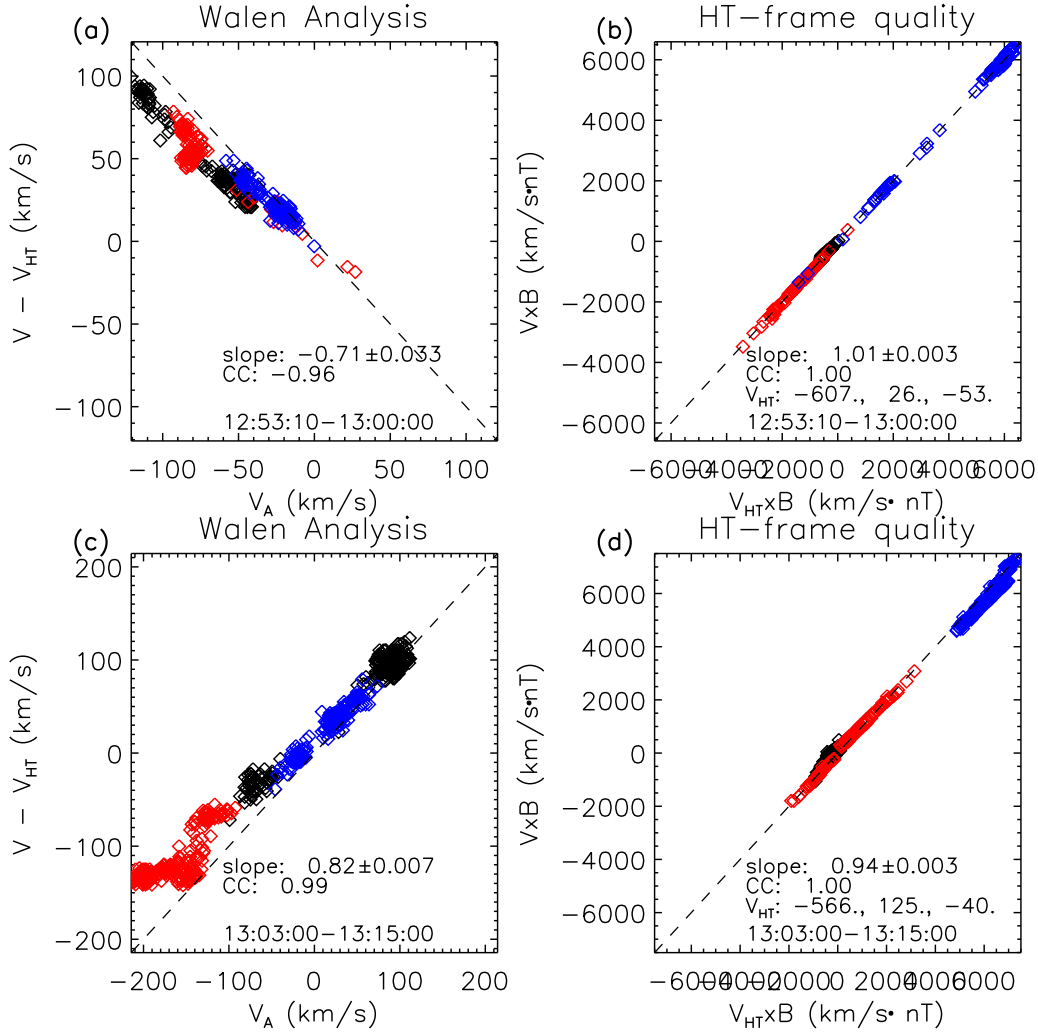
Figure 2. Walén analysis results of the two time intervals containing possible RDs (12:53:10–13:00:00 and 13:03:00–13:15:00). Comparison between V_A and $V - V_{HT}$ shows the good anti-correlation and correlation for the Earthside and sunside RDs, respectively (black, red, and blue squares represent the scatter plots of the GSE-x, y, and z components). Both of these two HT frames are in good quality with the $V_{HT} \times B$ and are almost the same as $V \times B$.

field components (Figure 1(b)) and in the proton bulk velocity components (Figure 1(c))—the jumps are marked with two vertical blue dashed lines and a vertical red dashed line on each side. Walén analysis of the negatively and positively correlated dB] and dV jumps on each side confirms the existence of a pair of RDs (see Figure 2). The slope and correlation coefficient for Walén that test for the preceding RD are calculated to be -0.74 ± 0.02 and 0.95, respectively. The relation between local V_A and $V - V_{HT}$ of the trailing RD is found to have a slope of $+0.76 \pm 0.03$ and a correlation coefficient of 0.94. Under the global Minimum Variance Analysis (MVA; Sonnerup & Scheible 1998), B_N is quite small, indicating that the RDs propagate upstream of the exhaust region very slowly in the N-direction. In the L and M directions, the magnetic field line kinks of the RDs may move much faster at a substantial fraction of Alfvén speed. This MVA analysis was verified to be insensitive to the choice of the time interval as long as all of the discontinuities were included appropriately in the time interval.

From the time sequences of proton density (N_P) and temperature (T_P) across the reconnection exhaust (Figures 1(f) and (g)), one may identify four regions (from left to right): there are two distinct regions of dense, cool plasmas separated by a transition (region 1 and region 2), and two distinct sparse, warm

plasmas, also separated by a transition (region 3 and region 4). Across the interface between regions 1 and 2, one can see a decrease in $|B|$, an increase in N_P and T_P, as well as an approaching to zero of B_L. This finite-width interface is inferred to be a possible SS according to the MHD Rankine–Hugonoit conservation relation analysis (Koval & Szabo 2008; Wilson et al. 2013). Similarly, the interface between regions 3 and 4 may also be classified as another SS. The upstream and downstream velocities in the shock frames on the two sides of the exhaust are ($U_{up,region-1} \sim 31\ km\,s^{-1}$, $U_{down,region-2} \sim 21\ km\,s^{-1}$) and ($U_{up,region-4} \sim 95\ km\,s^{-1}$, $U_{down,region-3} \sim 49\ km\,s^{-1}$), respectively. The angles between the normal direction and magnetic field direction are ($\theta_{BN,up,region-1} \sim 93°$, $\theta_{BN,down,region-2} \sim 97°$) and ($\theta_{BN,up,region-4} \sim 45°$, $\theta_{BN,down,region-3} \sim 41°$), respectively. This is only a rough estimate of the shock properties, which may not be highly accurate due to the significant deviation of plasma velocity distribution from local thermodynamic equilibrium, and due to the existence of compound discontinuities that are likely not in a steady state. The small changes of θ_{BN} between up- and downstreams of the shocks are due to their coexistence with RDs, for which the situation makes them look different from the traditional pristine slow shocks.
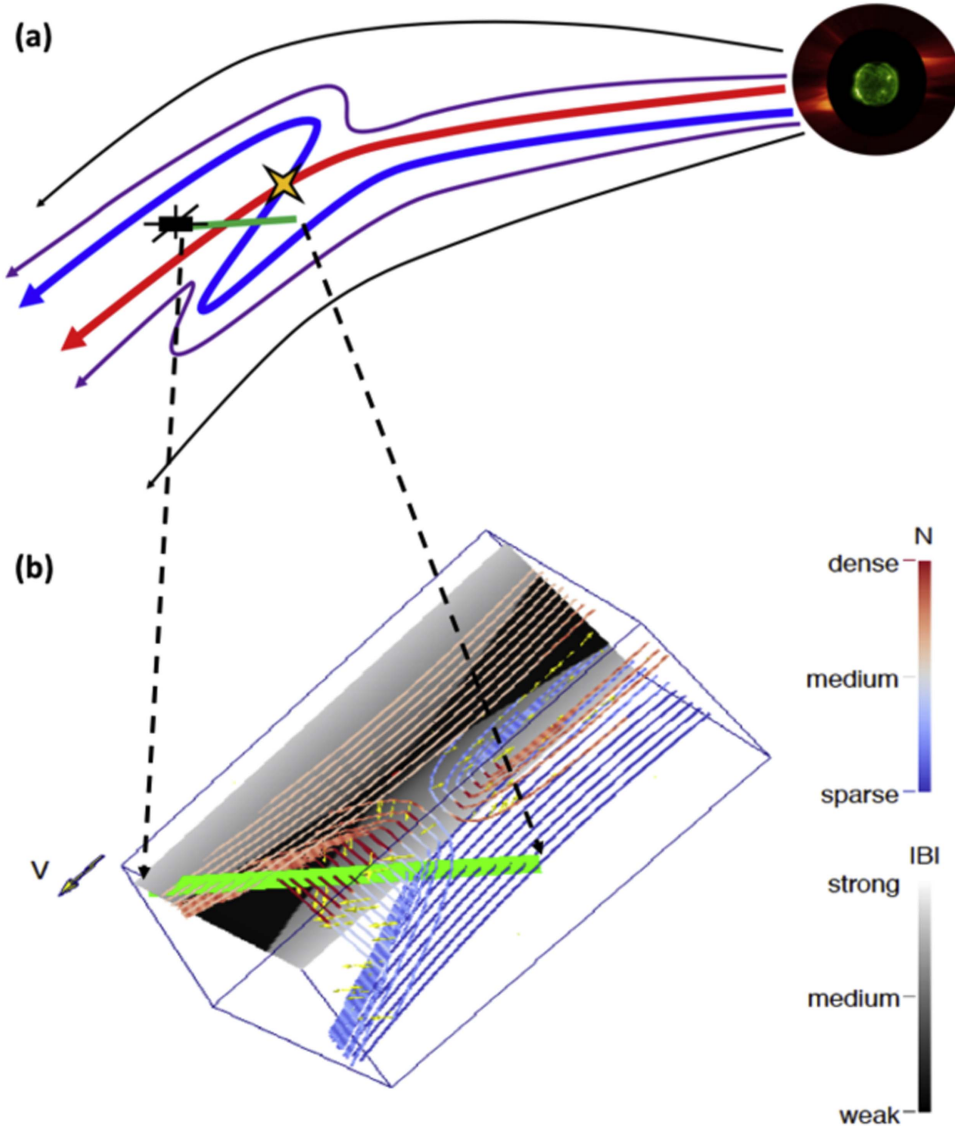
Figure 3. (a) Sketch illustrating the interchange reconnection between two interplanetary flux tubes (the more curved one with dense plasmas in red and the less curved one with tenuous plasmas in blue) with the same polarity at their footpoints on the Sun. The field lines involved in reconnection may be part of the complex system of ejecta. The composite images of the solar corona are obtained from the Extreme ultraviolet Imaging Telescope (EIT) in the Fe-195 Å channel and the LASCO-C2 coronagraph onboard the *SOHO* spacecraft. (b) A reconstruction of the magnetic reconnection region with asymmetric densities and temperatures on both sides of a possible contact interface, as measured by the *Wind* spacecraft along its trajectory (green bar). Bulk flow velocity vectors (yellow arrows) have V_L components away from the X-line and opposite V_M components toward the center of the exhaust region. The magnetic field vector is primarily aligned with B_L and B_M outside and inside of the reconnection exhaust region, respectively.

Therefore, the pair of back-to-back SSs seems to be concurrent with the pair of back-to-back RDs. The time interval between the RDs is about 10 minutes, which is equivalent to the length of the path across the exhaust region of about 50 Earth radii.

Across the interface between region 2 and region 3 (black vertical dashed line in Figure 1), there is a declining jump in N_P and a rising jump in T_P, maintaining roughly the same thermal pressure on either side. We do not see a dramatic jump in B and V components, although $|B|$ changes slightly across the interface. This interface is thus speculated to be a type of "contact interface" that keeps the two distinct materials relatively separate from one another. To see how the particles move and how the electric field self-consistently adapt around the interface, please refer to Section 2.3.

Proton thermal anisotropy, $\left(A_{\mathrm{th,p}} = \frac{T_{\perp \mathrm{p}}}{T_{\parallel \mathrm{p}}}\right)$, as derived from the *Wind*/3DP/PESA-low measurements, is found to be

smaller than 1 in the exhaust region (Figure 1(h)) where the proton parallel plasma beta ($\beta_{\parallel,\mathrm{p}}$) sees a dramatic increase (Figure 1(i)). This indicates a preferential parallel heating of protons in the exhaust region associated with a lesser increment in $T_{\perp \mathrm{p}}$. In Figures 1(h) and (i), the proton core and beam populations are treated as a whole when calculating $A_{\mathrm{th,p}}$ and $\beta_{\parallel,\mathrm{p}}$.

Pitch-angle distributions of electron differential flux density (*e*-flux) at two energy channels (47.5 and 228.2 eV) are illustrated in Figures 1(j) and (k). It is found that, in the exhaust region and especially in the downstream of cool and dense plasmas, there is a distinct enhancement of parallel and anti-parallel *e*-flux at the lower energy channels less than 150 eV. For the higher energies, the electrons are mainly travelling along the magnetic field line. Therefore, it is the lower energy rather than higher-energy electrons that may be trapped and
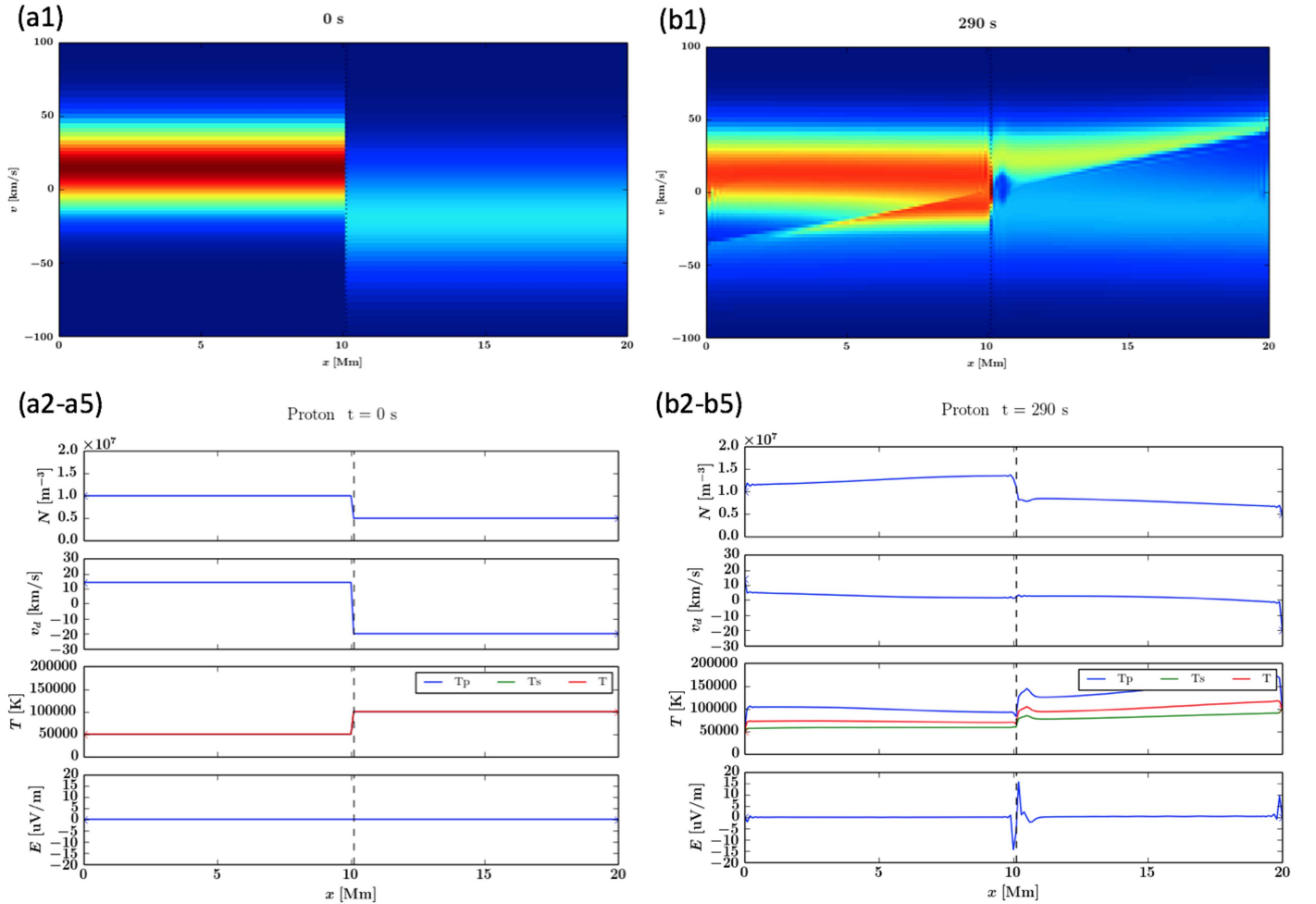
Figure 4. Time evolution of a contact interface in the hybrid simulation. Initial states of plasma and electric field are illustrated in panels (a1)–(a5): proton distribution in the phase space (a1), spatial profiles of proton number density (a2), proton bulk drift velocity (a3), proton temperature (parallel Tp, perpendicular Ts, average T) (a4), and zero electric field (a5). Evolution states of plasma and electric field at the time of 290 s are displayed in panels (b1)–(b5): deformed proton phase space density showing partial reflection at and partial penetration through the contact interface (b1), spatial profiles of proton number density (b2), reduced bulk velocity due to the mixing of the original and reflected/penetrated particles (b3), enhanced proton temperature especially the parallel component (b4), and bipolar electric field (b5).

energized by the magnetic field configuration and electric potential distribution within the exhaust region. The direction of the dominant suprathermal electron flux at higher energies indicates that the magnetic reconnection is an interchange reconnection between IMF lines with the same polarity on the Sun, rather than a reconnection between IMF lines of opposite polarities causing disconnection and strahl dropout (Gosling et al. 2005b) or a reconnection between traditional non-kinked open and closed IMF lines (Crooker et al. 2004).

2.2. Scenario of Interchange and Asymmetric Reconnection in a Global Context

The interchange reconnection between two IMF flux tubes with the same polarity at the solar surface is illustrated conceptually in Figure 3(a). The kinked IMF flux tube, which may be bent by non-uniform flow speeds or formed by an earlier reconnection at a lower altitude or a growing result of kink instability due to strong magnetic twist inside flux ropes (Zaqarashvili et al. 2014), tends to be interchange reconnected with the ambient and relatively straight flux tubes. The reconnection might also be within complex interplanetary coronal mass ejections (ICMEs) with the far-end loosely connected to the Sun due to the existence of asymmetric but still counter-streaming strahl electrons.

Figure 3(b) shows how the spacecraft passes through the magnetic reconnection exhaust configuration and what the jet flow velocity vectors look like. The change of state from (large $|B_L|$, small $|B_M|$) outside to (small $|B_L|$, large $|B_M|$) inside of the exhaust region is also illustrated. Flow velocity vectors, as denoted with yellow arrows, have two main components (V_L and V_M) in the exhaust region. The V_L component is the velocity of the jet flow as accelerated by the slingshot effect of the reconnected magnetic field lines (MFLs). The V_M component is mainly the result of the direction change of plasma momentum in the RD moving frame (one type of De Hoffmann–Teller (HT) frame; De Hoffmann & Teller 1950), in which both the upstream and downstream velocities are field-aligned and of similar magnitude. $|V_M|$ is approximately equal to V_A, since the RD is propagating mainly in the L-direction at about V_A with respect to the upstream plasma. In the reference frame of the downstream mean flow, V_M changes from one polarity to another polarity in the exhaust region.

2.3. Plasma Kinetics around an Evolving Contact Interface

This kind of contact interface is different from the MHD contact discontinuity, since the free penetration of protons across the interface in the collisionless space plasmas is
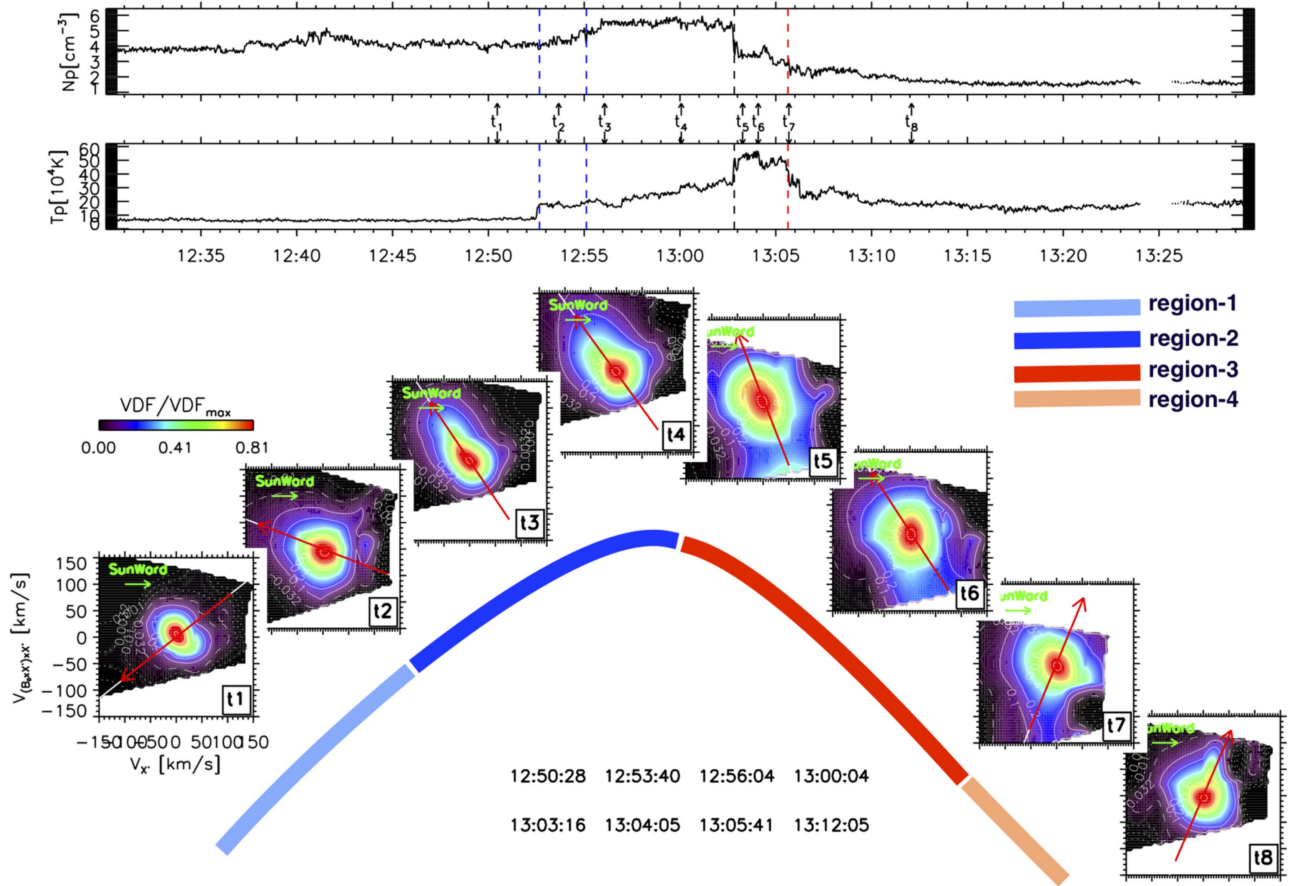
Figure 5. Snapshots of the proton velocity distribution function (p-VDF) at eight times inside and outside of the magnetic exhaust region, illustrating the signature of proton parallel heating in the exhaust region. The locations of the eight times are as follows: upstream (t1), transition (t2), downstream (t3, t4) of the cool and dense plasmas on one side of the contact interface; downstream (t5, t6), transition (t7), and upstream (t8) of the warm and tenuous plasmas on the other side of the contact interface. Time sequences of the density, $N_{\rm p}$, and temperature, $T_{\rm p}$, are plotted for reference.

partially held back by a self-consistent electric potential barrier developed around the interface according to kinetic simulation results (see Figure 4).

To see if the contact interface can be maintained somehow and the protons can be reflected back at the contact interface, a 1D hybrid simulation is conducted to model the time evolution of the contact interface. Note that, in the setup of hybrid simulation, proton kinetics are described with the Vlasov equation and electrons are approximated as a fluid (Ruan et al. 2016). This 1D model provides a rough, but qualitatively useful, approximation to the evolution of spatial distribution of plasma states along the N-direction in the distant exhaust region. Here we neglect the spatial inhomogeneity of magnetized plasmas in the L-dimension, which is assumed to be relatively uniform as compared to the N-dimension in the distant exhaust region far away from the reconnection site. This 1D approximation is inspired by Lin & Lee (1995), who utilized the 1D MHD and hybrid simulations to study the evolution of the reconnection exhaust region by solving the Riemann problem there. Our 1D model differs from the preceding works in introducing counter streams in the opposite directions on either side of the interface to mimic the downstream flows in the HT reference frame, which is moving basically along with the jet flow in the L-direction.

Initially, across the contact interface, there exists a thermal pressure balance between both sides, with a cool and dense plasma and a warm and tenuous plasma on the left and right

sides, respectively (see panels (a1), (a2), and (a4) in Figure 4). The plasmas on both sides are flowing in the opposite directions heading toward the contact interface. As the time evolves, a bipolar electric field (see (b5) in Figure 4) is formed, leading to a positive potential around the contact interface. This positive potential plays a role in reflecting the major part of protons back to their original incident sides, while leaving the other protons penetrating through the interface into the opposite side (see (b1) in Figure 4). By applying the moment analysis to the proton velocity distribution, the density and temperature are found to increase on both sides but still remain as a significant transition (imbalance) across the interface.

2.4. First Step of Energy Conversion: Energization of Protons and Electrons

The proton heating signature in the exhaust region is illustrated in Figure 5. Eight snapshots of p-VDF are aligned in position to follow the MFL configuration. The p-VDFs at (t1), (t2), (t3, t4) are upstream of the cool and dense plasmas in the transition layer, and in the deep downstream of the cool and dense plasmas, respectively. From the upstream to the downstream, the p-VDF experiences a significant change: development of a beam population parallel to B_0, with the core population heading toward the contact interface. On the other side of the contact interface, the p-VDFs downstream and upstream of the warm and sparse plasmas are displayed in panels
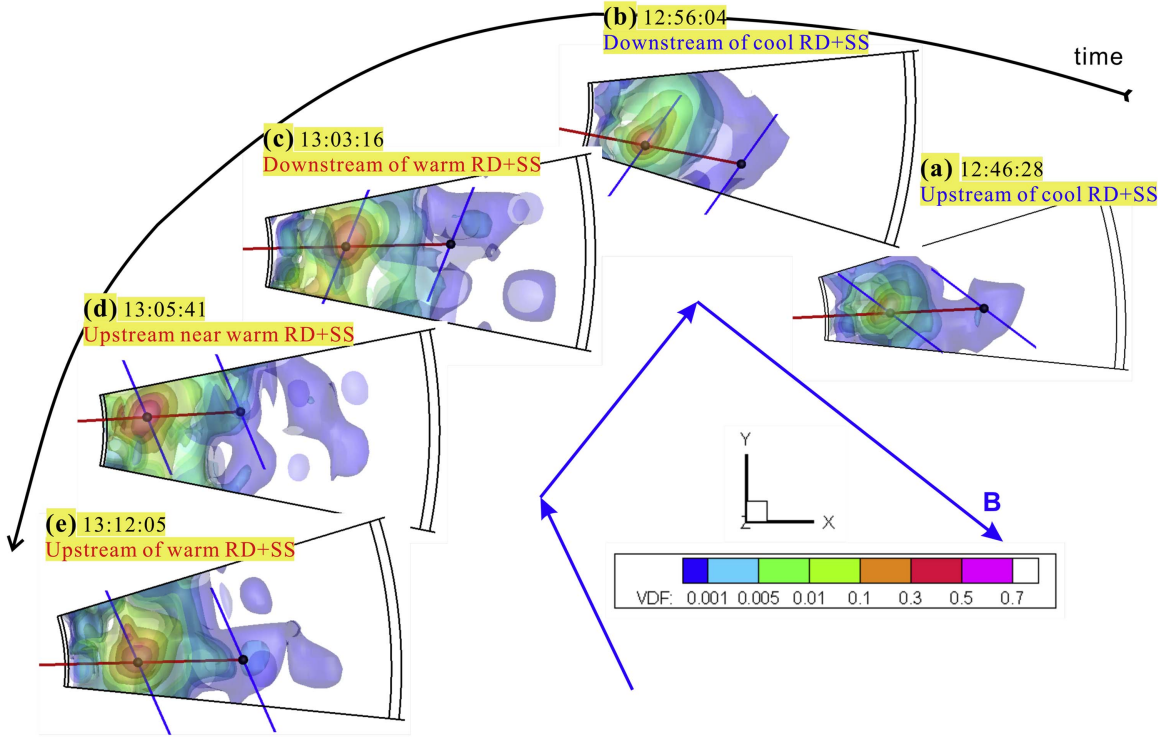
Figure 6. 3D phase space density of ion particles inside and outside of reconnection exhaust region. The red line in each panel starts from the zero velocity and passes through the velocity vector with the maximum proton phase space density. The blue lines in each panel represent the magnetic field direction passing through the velocity positions of $V|_{VDF(proton)=max}$ and $\sqrt{2}\,V|_{VDF(proton)=max}$, respectively. Ideally, if the alpha particles were co-moving with the protons at the same velocity without any relative drift, the velocity vector for the maximum phase space density of alpha particles (without distinguishing the m/q ratio) would be the same as $\sqrt{2}\,V|_{VDF(proton)=max}$. Note that the m/q ratio for the particles measured by an electrostatic analyzer without time-of-flight technique is assumed to be the same. Along with the time, the WIND spacecraft were recording the phase space densities of particles in different regions: upstream of cool RD+SS (a compound structure of rotational discontinuity and slow shock) (a), downstream of cool RD+SS (b), downstream of warm RD+SS (c), and upstream of warm RD+SS (d) and (e).

(t5)–(t8). The p-VDFs at (t5, t6) have two populations with the main population drifting along the field toward the contact interface and the second population toward the compound structure of RD and SS. The relative drift between the primary and secondary populations at (t5, t6) is larger than that at (t3, t4), causing part of the second population to extend beyond the measured range.

The core + beam p-VDF in the exhaust region is commonly called a dumbbell distribution if the two components are well detached from and comparable to one another. It is interesting that the p-VDFs show different patterns on both sides of the contact interface. It is expected that the HT (propagating RD) frame is moving mainly along with the jet flow in the L-direction. The upstream plasma in the HT frame moves toward the discontinuity at about V_A, and turns to follow the field line direction in the downstream exhaust region with a slight slow-down in speed due to the higher thermal pressure downstream. Traditionally, in the exhaust region of symmetric reconnection, the major core population may be the plasmas coming from the nearest upstream, while the minor beam population may be from the upstream on the other side. However, in our case with reconnection between asymmetric plasmas, the beam population on one side of the contact interface is distinctly different in the thermal state from the core population on the other side, yet similar to the core population on the same side. Therefore, the beam (second) population might be attributable to reflection at the contact interface by some electric potential barrier yet to be measured and confirmed.

Note that coordinate origin of the proton-VDFs in Figure 5 has been translated to the velocity position with maximum phase space density from the original velocity position of the spacecraft, which can be approximated as static when compared to the supersonic solar wind flow. To illustrate the difference of both bulk velocity and thermal state between the upstream and downstream of the exhaust region, we present the original 3D-VDFs in Figure 6. The VDFs of α particles are also recorded in the figure, showing remarkable expansion of the contour surfaces in the exhaust region, similar to that of protons. The velocity for α particles in the figure is just derived with the proton's mass-to-charge ratio without adopting its real mass-to-charge ratio.

The electron velocity distribution function (e-VDF) illustrated in Figure 7 also shows a clear signature of the parallel heating of its core component in the exhaust region. As a result of the preferential parallel heating, the pitch-angle distribution of the differential flux density at energies lower than 200 eV is mainly concentrated around 0° and 180° (Figure 1(j)). For the electrons above 200 eV, which do not show a difference in e-VDF between the exhaust and ambient region, they seem not to be affected and trapped by the speculated electric potential. The same dominant direction of the asymmetric, but still counter-stream, strahl electrons above 200 eV (parallel to local B_0) throughout the upstream and downstream regions indicates the nature of the interchange reconnection between two IMF flux tubes (probably affiliated with a complex B-field system involving ICME) with the same (positive) polarity of their near-end footpoints on the Sun. Note that the existence of
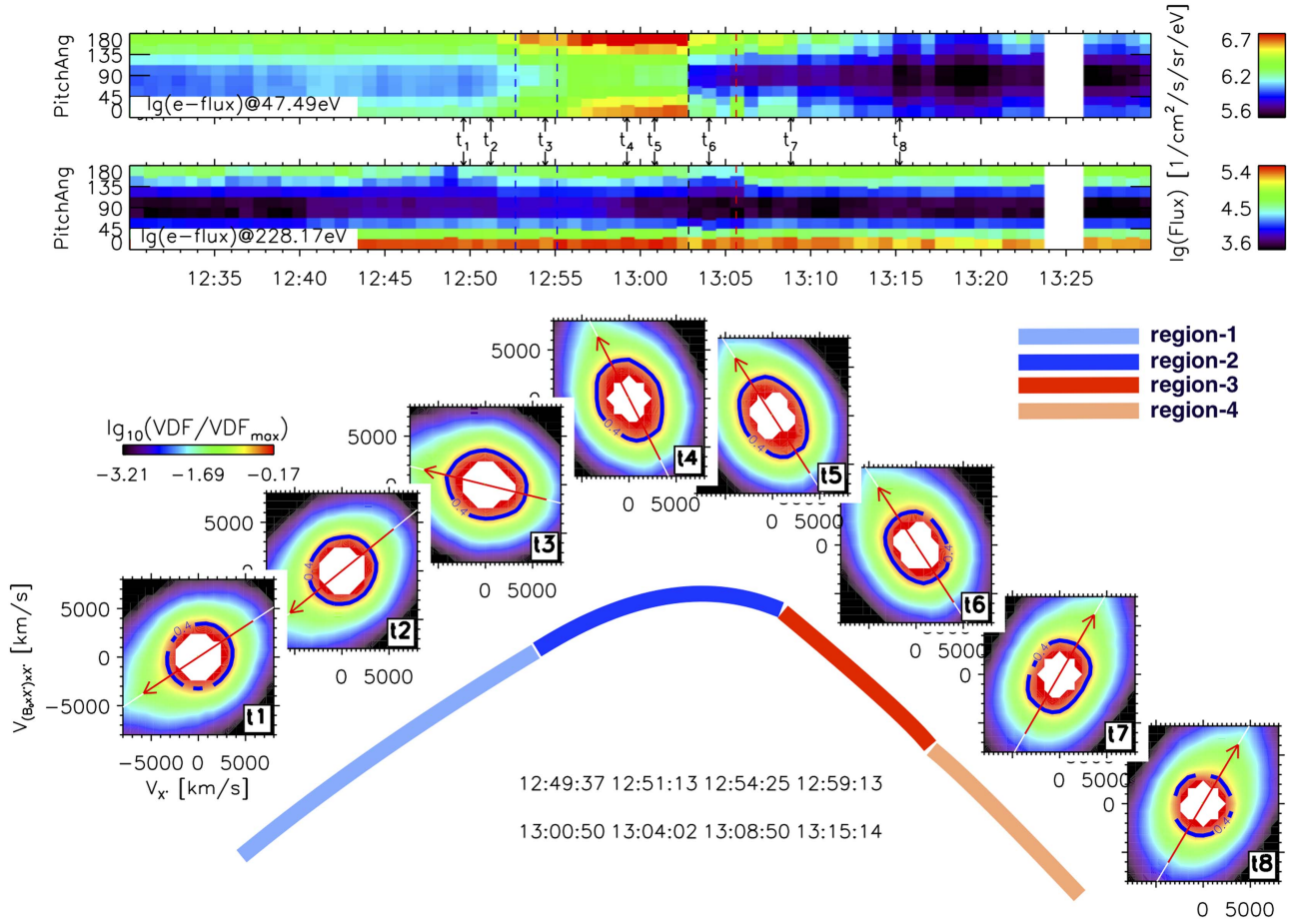
Figure 7. Eight snapshots of electron velocity distribution function (*e*-VDF) inside and outside of the magnetic exhaust region, showing the parallel heating of thermal electrons as characterized with the field-aligned elongation of the blue contours (*e*-VDF/*e*-VDF$_{max}$ = 0.4). The snapshots are located at upstream (t1), (t2), transition (t3), downstream (t4), (t5) on the left side of the contact interface and downstream (t6), transition (t7), upstream (t8) on the right side of the contact interface. The thermal part of the *e*-VDF is more anisotropic inside and more isotropic outside of the exhaust region, while the suprathermal strahl part of the *e*-VDF seems unaffected by the reconnection exhaust. The different behaviors of thermal and suprathermal electrons are also illustrated in their pitch-angle distribution of differential flux density at the corresponding energy channels of about 47 eV and 228 eV, respectively.

weak, field-aligned proton heat flux in the upstreams on both sides of the exhaust region, as discerned from the measurements by the 3DP and *Solar Wind Experiment* (SWE) instruments, also indicates the same polarity of near-end footpoints for these two flux tubes.

### 2.5. Second Step of Energy Conversion: Wave Excitation and Turbulence Enhancement

Besides the RDs with steps of correlated/anti-correlated jumps mainly in B_L and V_L components, the fluctuations in other time intervals show a good sense of Alfvénic correlations as well, which are illustrated in Figures 8(a)–(c) showing the cross-correlation spectra of (B_L, V_L), (B_M, V_M), and (B_N, V_N). For example, B_N and V_N are highly anti-correlated on the cool and dense side of the contact interface, while in positive correlation they are on the warm and sparse side. Unlike the single step of jump in B_L and V_L across the RD, the B_N and V_N components oscillate in large amplitude over several cycles near the RD. These features indicate that Alfvén waves, besides the RDs, are propagating in the opposite direction on the either side of the contact interface. There seems to be a wave source near the contact interface, emanating Alfvénic fluctuations outward. The Alfvén waves generated in the exhaust region are

stronger in power spectral density (PSD) than those in the ambient undisturbed regions (see Figure 9).

The free energy to generate these Alfvénic fluctuations may come from the plasma kinetic energy through a certain instability mode, e.g., the magnetic firehose instability (Bale et al. 2009; Maruca et al. 2012; Klein 2017). The magnetic tension can be reduced in the plasma with large $T_\parallel/T_\perp$ and/or with relative drift between multi-components/multi-species. As a consequence, the MFL is subject to oscillating deformation and propagating waves. Patchy regions of firehose unstable plasma have been measured in exhausts in the Earth's magnetotail (Hietala et al. 2015). Those studies did not, however, present evidence of excited waves. As illustrated in Figure 5, the *p*-VDFs with a dumbbell shape may be prone to the firehose instability. Since the 3DP/PESA-low cannot record the full *p*-VDF at some times, we adopt the parameters of protons and alpha particles derived from the SWE measurements (Kasper et al. 2002; Stevens & Kasper 2007). We calculate $\Lambda_f = \sum_s \frac{P_{\parallel,s} + \rho_s v_{d,s}^2 - P_{\perp,s}}{2 \cdot P_B}$, a parameter that indicates long-wavelength firehose instability when it takes a value greater than 1 (Chen et al. 2016), based on the magnetic pressure, P_B, and the parameter sets (mass density, ρ_s, drift velocity, $v_{d,s}$, and parallel and perpendicular thermal pressure, $P_{\parallel,s}$ & $P_{\perp,s}$) of various species denoted as s (proton core, proton
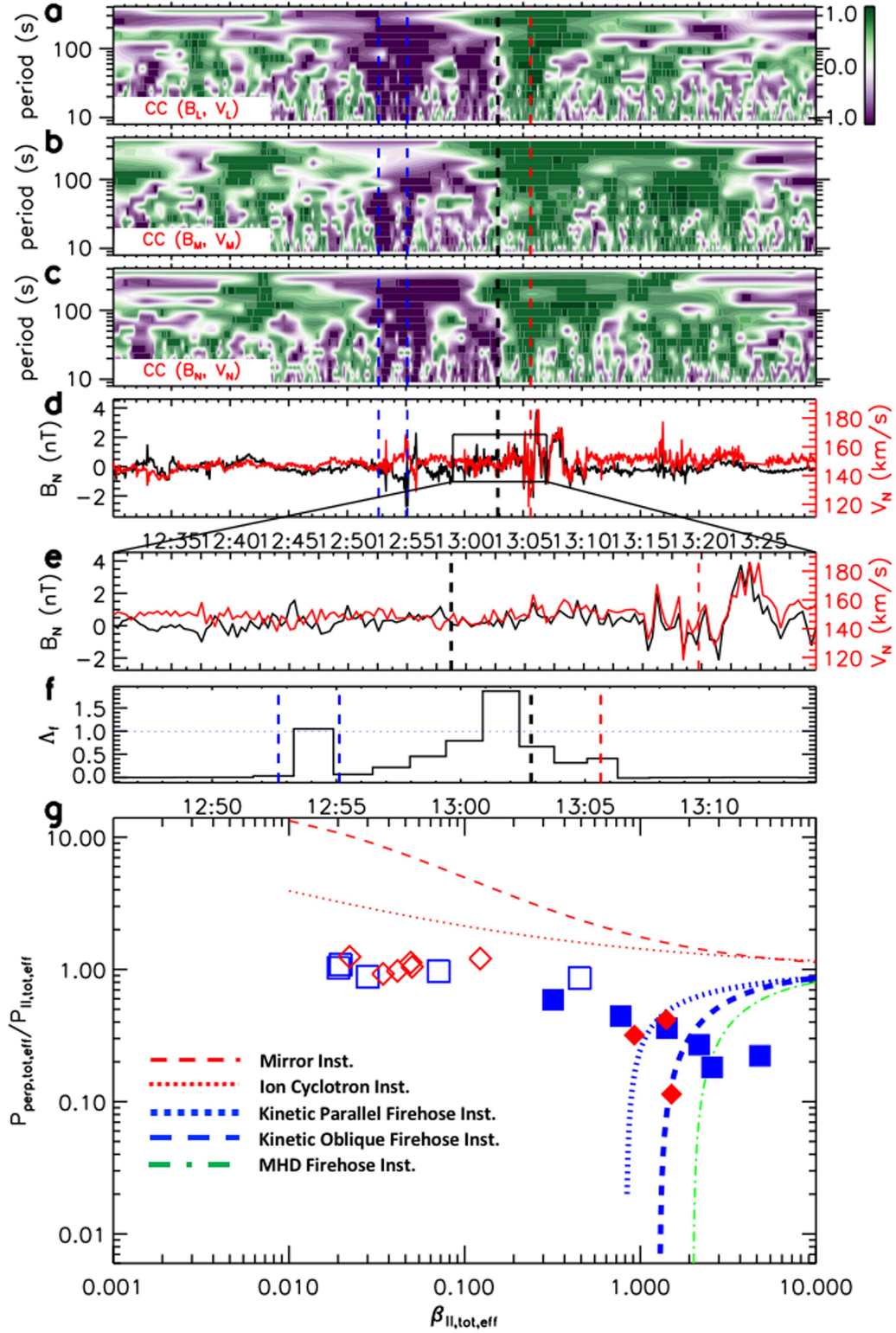
Figure 8. Evidence of Alfvénic fluctuations excited and emanated from the exhaust region due to firehose instability in the parallel energized plasmas. Cross-correlation spectra of (B_L, V_L), (B_M, V_M), and (B_N, V_N) are illustrated in panels (a), (b), and (c), respectively. The two RDs on the left side (two blue dashed vertical lines) have positive correlation sense (dark purple), while the right RD (red dashed vertical line) is characterized by a negative correlation (dark green). On either side of the contact interface there also exist Alfvénic fluctuations with opposite correlation sense, indicating a divergent propagation away from the contact interface (see the transition between dark purple and dark green around the black dashed vertical line in (d), and the time sequences of (B_N, V_N) in (e)). The firehose instability parameter, Λ_f, a sum of the contributions from parallel thermal pressure and field-aligned drift of the protons and alpha particles, is plotted in panel (f). The parameter set $\left(\beta_{\parallel,p+\alpha,\mathrm{eff}}, \frac{P_{\perp,p+\alpha,\mathrm{eff}}}{P_{\parallel,p+\alpha,\mathrm{eff}}}\right)$ during the whole time interval is scatter plotted in (g) as different types of symbols (hollow and solid blue rectangles for the upstream and downstream of the cool side, hollow and solid red diamonds for the upstream and downstream of the warm side). The thresholds of various plasma instabilities are plotted for comparison: blue dashed line (kinetic oblique firehose), blue dotted line (kinetic parallel firehose), green dotted–dashed line (fluid firehose), red dashed line (mirror), and red dotted line (ion cyclotron).
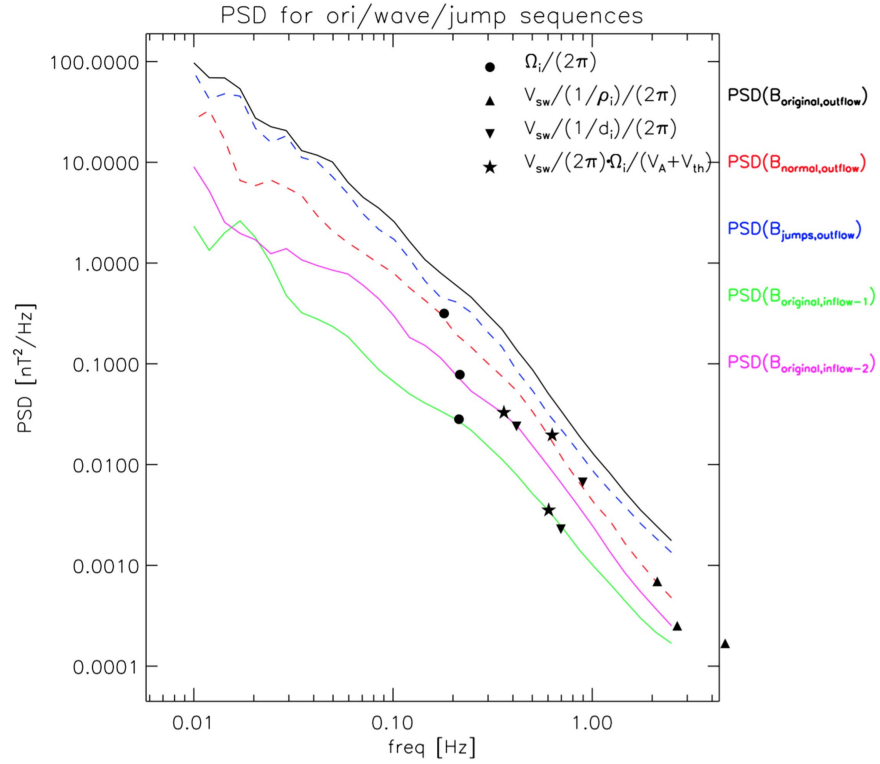
Figure 9. Power spectral density profiles of magnetic field fluctuations in different regions: (black solid) exhaust region with discontinuity jumps taken into account, (red dashed) exhaust region with discontinuity jumps excluded, (blue dashed) just focusing on the discontinuity jumps and the fluctuations of the intervals between are set zero, (green line) upstream region of cold and dense plasmas, (magenta line) and upstream region of warm and tenuous plasmas. Four scales are also illustrated for the comparison with the spectral break position. The four scales are proton cyclotron frequency (solid circle), Doppler-shifted frequencies for the ion gyro-radius (solid upper triangle), ion inertial length (solid lower triangle), and the ion cyclotron resonance scale (solid pentagram) in the spacecraft frame.

beam, and alpha particle). The time sequence of Λ_f is plotted in Figure 8(f), which shows that Λ_f is larger than 1 at two moments in time, with the largest one being close to the contact interface. We also scatterplot the ion (protons and α particles) plasma parameters ($\beta_{\parallel,\mathrm{p}+\alpha,\mathrm{eff}}$, $\frac{P_{\perp,\mathrm{p}+\alpha,\mathrm{eff}}}{P_{\parallel,\mathrm{p}+\alpha,\mathrm{eff}}}$) and compare them with the instability thresholds, finding that the downstream plasma conditions (red solid diamonds and blue solid squares for warm and cool downstreams, respectively) are closer to or even beyond the threshold of firehose instability (Hellinger et al. 2006). The threshold formulas of ($\beta_{\parallel}$, $\frac{P_{\perp}}{P_{\parallel}}$) for MHD, kinetic parallel, and kinetic oblique firehose instabilities are $A = 1 - \frac{1}{\beta_{\parallel}}$, $A = 1 - \frac{0.47}{(\beta_{\parallel} - 0.59)^{0.53}}$, and $A = 1 - \frac{1.4}{(\beta_{\parallel} + 0.11)^{1.0}}$, respectively (Hellinger et al. 2006). The effective parallel plasma beta, $\beta_{\parallel,\mathrm{p}+\alpha,\mathrm{eff}}$, is calculated with $\beta_{\parallel,\mathrm{p}+\alpha,\mathrm{eff}} = \frac{P_{\parallel,\mathrm{pc}} + \rho_{\mathrm{pc}} \cdot v_{d,\mathrm{pc}}^2}{P_B} + \frac{P_{\parallel,\mathrm{pb}} + \rho_{\mathrm{pb}} \cdot v_{d,\mathrm{pb}}^2}{P_B} + \frac{P_{\parallel,\alpha} + \rho_{\alpha} \cdot v_{d,\alpha}^2}{P_B}$, where the subscripts "pc," "pb," and "α" represent the proton core, proton beam components, and alpha particles, respectively, and the drift velocities are with respect to the mass center of the proton core, proton beam, and alpha population. The effective pressure anisotropy is determined by $\frac{P_{\perp,\mathrm{p}+\alpha,\mathrm{eff}}}{P_{\parallel,\mathrm{p}+\alpha,\mathrm{eff}}} = \frac{P_{\perp,\mathrm{pc}} + P_{\perp,\mathrm{pb}} + P_{\perp,\alpha}}{(P_{\parallel,\mathrm{pc}} + \rho_{\mathrm{pc}} \cdot v_{d,\mathrm{pc}}^2) + (P_{\parallel,\mathrm{pb}} + \rho_{\mathrm{pb}} \cdot v_{d,\mathrm{pb}}^2) + (P_{\parallel,\alpha} + \rho_{\alpha} \cdot v_{d,\alpha}^2)}$.

3. Summary and Discussion

The evidence for plasma energization in the reconnection exhaust are presented here, showing the signature of preferential parallel heating as characterized with the dumbbell-shaped p-VDF and the field-aligned elongated e-VDF.

Furthermore, the derived plasma parameters are found to be locally firehose unstable in the exhaust, suggesting that the instability may be responsible for the enhanced PSD level of magnetic turbulence and the opposite propagation of Alfvenic waves away from the contact interface. The plasmas are asymmetric, with a cool and dense plasma on one side and a warm and sparse plasma on the other side of the contact interface. We hypothesize that there may be an electric potential barrier (yet to be detected in future missions) formed around the contact interface, which partly prevents the free penetration of protons and energizes the trapped electrons.

The energized plasmas, which store excess free energy, are not the ultimate deposit of converted energy. Instead, they become firehose unstable and excite waves. The emanation of Alfvén waves in the second step of energy conversion might be the source of sunward propagating Alfvén waves recently identified in the solar wind (He et al. 2015; Li et al. 2016). Magnetic reconnection was traditionally thought to occur between the IMF lines with the opposite polarities on the solar surface (Gosling et al. 1995; Huang et al. 2016). It is newly suggested that curved IMF lines with the same polarity on the Sun can also be reconnected even at 1 au, interchanging their footpoints. This discovery expands the applicability of magnetic reconnection inflow tubes stemming from the areas of the same polarity.

This study highlights that the reconnection exhaust region in the interplanetary space, which may extend over tens of Earth radii (much larger than the ion diffusion region of about 100 km), is an important site where plasma heating and wave excitation are taking place in association with the bulk jet flows. These insights help to understand (a) the complex physical processes (multiple steps of energy conversion) as

triggered by the reconnection, (b) the application of energy conversion in the exhaust to the plasma heating and turbulence development in various environments, and (c) the spectroscopic diagnosis of the multi-component line profiles emitting from the flare sites on astronomical bodies.

ORCID iDs

He Jiansen ⓘ https://orcid.org/0000-0001-8179-417X
Stevens Michael ⓘ https://orcid.org/0000-0002-7728-0085
Li Hui ⓘ https://orcid.org/0000-0002-4839-4614
Tu Chuanyi ⓘ https://orcid.org/0000-0002-9571-6911

References

Aschwanden, M. J., Kosugi, T., Hanaoka, Y., Nishio, M., & Melrose, D. B. 1999, ApJ, 526, 1026
Bale, S. D., Kasper, J. C., Howes, G. G., et al. 2009, PhRvL, 103, 211101
Birn, J., Drake, J. F., Shay, M. A., et al. 2001, JGR, 106, 3715
Chen, C. H. K., Matteini, L., Schekochihin, A. A., et al. 2016, ApJL, 825, L26
Crooker, N. U., Antiochos, S. K., Zhao, X., & Neugebauer, M. 2012, JGRA, 117, A04104
Crooker, N. U., Huang, C.-L., Lamassa, S. M., et al. 2004, JGRA, 109, A03107
De Hoffmann, F., & Teller, E. 1950, PhRv, 80, 692
Deng, X. H., & Matsumoto, H. 2001, Natur, 410, 557
Drake, J. F., Swisdak, M., Phan, T. D., et al. 2009, JGRA, 114, A05111
Eastwood, J. P., Phan, T. D., Øieroset, M., & Shay, M. A. 2010, JGRA, 115, A08215
Egedal, J., Daughton, W., & Le, A. 2012, NatPh, 8, 321
Egedal, J., Fox, W., Katz, N., et al. 2008, JGRA, 113, A12207
Eriksson, S., Øieroset, M., Baker, D. N., et al. 2004, JGRA, 109, A10212
Fujimoto, K., & Sydora, R. D. 2008, GeoRL, 35, L19112
Gosling, J. T., Birn, J., & Hesse, M. 1995, GeoRL, 22, 869
Gosling, J. T., Phan, T. D., Lin, R. P., & Szabo, A. 2007, GeoRL, 34, L15110
Gosling, J. T., Skoug, R. M., McComas, D. J., & Smith, C. W. 2005a, JGRA, 110, A01107
Gosling, J. T., Skoug, R. M., McComas, D. J., & Smith, C. W. 2005b, GeoRL, 32, L05105
He, J. S., Pei, Z., Wang, L., et al. 2015, ApJ, 805, 176
Hellinger, P., Trávníček, P., Kasper, J. C., & Lazrus, A. J. 2006, GeoRL, 33, 9101
Hietala, H., Drake, J. F., Phan, T. D., Eastwood, J. P., & McFadden, J. P. 2015, GeoRL, 42, 7239
Huang, C., Lu, Q., Guo, F., et al. 2015, GeoRL, 42, 7282
Huang, J., Liu, Y. C. M., Klecker, B., & Chen, Y. 2016, JGRA, 121, 19
Huang, S. Y., Zhou, M., Sahraoui, F., et al. 2012, GeoRL, 39, L11104
Huttunen, K. E. J., Bale, S. D., Phan, T. D., Davis, M., & Gosling, J. T. 2007, JGRA, 112, A01102
Innocenti, M. E., Goldman, M., Newman, D., Markidis, S., & Lapenta, G. 2015, ApJL, 810, L19
Kasper, J. C., Lazarus, A. J., & Gary, S. P. 2002, GeoRL, 29, 1839
Klein, K. G. 2017, PhPl, 24, 055901
Koval, A., & Szabo, A. 2008, JGRA, 113, A10110
Li, H., Wang, C., Belcher, J. W., He, J., & Richardson, J. D. 2016, ApJL, 824, L2
Lin, C. C., Feng, H. Q., Chao, J. K., et al. 2008, JGRA, 113, A01101
Lin, Y., & Lee, L. C. 1995, JGR, 100, 19227
Liu, Y. H., Drake, J. F., & Swisdak, M. 2011, PhPl, 18, 062110
Maruca, B. A., Kasper, J. C., & Gary, S. P. 2012, ApJ, 748, 137
Øieroset, M., Phan, T. D., & Fujimoto, M. 2004, GeoRL, 31, L12801
Osman, K. T., Matthaeus, W. H., Gosling, J. T., et al. 2014, PhRvL, 112, 215002
Petschek, H. E. 1964, in Physics of Solar Flares, ed. W. N. Hess (NASA SP-50; Washington, DC: NASA), 425
Phan, T. D., Gosling, J. T., Davis, M. S., et al. 2006, Natur, 439, 175
Phan, T. D., Gosling, J. T., & Davis, M. S. 2009, GeoRL, 36, L09108
Pulupa, M. P., Salem, C., Phan, T. D., Gosling, J. T., & Bale, S. D. 2014, ApJL, 791, L17
Ruan, W., He, J., Zhang, L., et al. 2016, ApJ, 825, 58
Sonnerup, B. U. 1979, in Solar System Plasma Physics, ed. L. J. Lanzerotti, C. F. Kennel, & E. Newman Parker (Amsterdam: North-Holland), 45
Sonnerup, B. U., & Scheible, M. 1998, ISSIR, 1, 185
Stevens, M. L., & Kasper, J. C. 2007, JGRA, 112, A05109
Vörös, Z., Baumjohann, W., Nakamura, R., et al. 2004, JGRA, 109, A11215
Vörös, Z., Sasunov, Y. L., Semenov, V. S., et al. 2014, ApJL, 797, L10
Weygand, J. M., Kivelson, M. G., Khurana, K. K., et al. 2005, JGRA, 110, A01205
Whang, Y. C., Zhou, J., Lepping, R. P., et al. 1998, JGR, 103, 6513
Wilson, L. B., Koval, A., Sibeck, D. G., et al. 2013, JGRA, 118, 957
Zaqarashvili, T. V., Vörös, Z., Narita, Y., & Bruno, R. 2014, ApJL, 783, L19